



Pulsating nanofluids jet impingement cooling of a heated horizontal surface



Fatih Selimefendigil ^{a,*}, Hakan F. Öztöp ^{b,1}

^a Department of Mechanical Engineering, Celal Bayar University, TR-45140 Manisa, Turkey

^b Department of Mechanical Engineering, Technology Faculty, Firat University, Elazığ, Turkey

ARTICLE INFO

Article history:

Received 8 May 2013

Received in revised form 2 October 2013

Accepted 3 October 2013

Available online 31 October 2013

Keywords:

Nanofluids

Pulsating impinging jet

Heat transfer augmentation

ABSTRACT

In this study, a numerical study of pulsating rectangular jet with nanofluids is presented. The aim of this work is to numerically investigate the effects of various parameters such as pulsating frequency, Reynolds number, nanoparticle volume fraction on the fluid flow and heat transfer characteristics. The unsteady Navier–Stokes and energy equations are solved with a commercial finite volume based code. It is observed in the steady case, adding nanoparticles increases the peak value of the Nusselt number at the stagnation point and spatial-averaged Nusselt number along the impingement plate. Heat transfer enhancement up to 18.8% is obtained for particle volume fraction of 6% at Reynolds number of 200. In the pulsating flow case, the combined effect of pulsation and inclusion of nanoparticles is not favorable for the augmentation of the stagnation point Nusselt number at $Re = 200$, $\phi = 1\%$, 3% and at $Re = 400$, $\phi = 1\%$, 3% when compared to the steady case.

© 2013 Elsevier Ltd. All rights reserved.

1. Introduction

Impinging jets find a vast amount of industrial application areas such as thermal treatment of surfaces, drying of textiles and papers, annealing of glass, cooling of electronic devices, turbine blades and outer walls of combustors. A jet of fluid from a slot or a circular hole is directed towards a targeted surface. High values of the local heat and mass transfer coefficients can be obtained with impinging jets. Many studies have been conducted on impinging jets for circular and slot jets with or without moving impinging surface. The flow field and thermal characteristics are different in slot jets compared to circular jets. The heat transfer analysis of impingement jets are considerably complicated due to flow recirculation, pressure gradients and local thinning of the boundary layer on the impingement surface. A review for the heat transfer data of circular jet impingement in turbulent flow was given by Jambunathan et al. [1]. A comprehensive survey for single phase liquid jets was presented in Webb and Ma [2]. The hydrodynamics of impinging gas jets with heat and mass transfer variables and boundary conditions were reviewed in Martin [3]. A theoretical investigation of impingement heat transfer with single phase free slot jet was carried out by Chen et al. [4]. They divided the thermal and velocity boundary layer into four regions of flow from

which they obtained correlations for the heat transfer coefficients. Numerical studies of impinging jets were carried out by many researchers. Lee et al. [5] have numerically studied the heat transfer in a confined impinging jet using the finite volume method in the unsteady regime. They studied the effects of Reynolds number and height ratio on the flow and thermal field. They noted that beyond a critical Reynolds number which depends on height ratio the flow field shows unsteady behavior. Park et al. [6] have numerically analyzed the two-dimensional confined impinging slot jet using finite element method. Both the laminar and turbulent jets have been studied. Chiriac and Ortega [7] have used a finite difference method to calculate the flow and thermal field in a confined two dimensional slot jet impinging on an isothermal plate for a range of Reynolds number between 250 and 750 and for a fixed jet to plate spacing. They reported that the flow field becomes unsteady for Reynolds number between 585 and 610 and the unsteady jet showed a peak frequency that corresponds to the formation of shear layer vortices at the jet exit. Lou et al. [8] have studied the effects of geometric parameters (nozzle width, nozzle to plate spacing) on the confined impinging jet heat transfer for Reynolds number between 26 and 1000, numerically. They noted that with the decrease of nozzle width and nozzle-to-plate spacing, heat transfer coefficient decreases and surface roughness generally deteriorates laminar impinging jet heat transfer. Sharif and Banerjee [9] have numerically investigated the heat transfer due to confined slot-jet impingement on a moving plate. The turbulence model was included with k – ϵ model and enhanced wall treatment. They studied the effects of Reynolds number, moving

* Corresponding author. Tel.: +90 236 241 21 44; fax: +90 236 241 21 43.

E-mail addresses: fatih.selimefendigil@cbu.edu.tr (F. Selimefendigil), hfoztot1@gmail.com (H.F. Öztöp).

¹ Tel.: +90 424 2370000x4222.

Nomenclature

A	amplitude of the pulsating jet inlet velocity
D_h	hydraulic diameter (m)
f	frequency of the pulsating jet velocity (Hz)
H	nozzle to plate spacing (m)
h	local heat transfer coefficient ($\text{W/m}^2 \text{K}$)
k	thermal conductivity (W/m K)
L	plate length (m)
Nu	local Nusselt number, hH/k
p	pressure (Pa)
Pr	Prandtl number, $\frac{\nu}{\alpha}$
Re	Reynolds number, $\frac{u_0 2W}{\nu}$
T	temperature (K)
t	time (s)
u, v	x – y velocity components (m/s)
W	slot width (m)
x, y	Cartesian coordinates (m)

Greek Characters

α	thermal diffusivity (m^2/s)
ν	kinematic viscosity (m^2/s)
ρ	density of the fluid (kg/m^3)
τ	oscillation period (s)
ϕ	particle volume fraction

Subscripts

bf	base fluid
c	cold
h	hot
m	mean
nf	nanofluid
p	particle
s	steady state
$stag$	stagnation point

plate velocity and distance of separation between the impinging plate and jet exit. They observed that the average Nusselt number increases with the jet exit Reynolds number and plate velocity, but the average skin friction coefficient increases only with the plate velocity. Varol et al. [10] have numerically studied the two-dimensional slot impingement onto two heated cylinder with different diameters for turbulent flow. The effects of Reynolds number, diameter ratio of the cylinders and the ratio of the distance between the cylinders to slot jet height on the fluid flow and heat transfer were investigated. It was found that the diameter ratios of the cylinder can be used as a control element for heat transfer. Dagtekin and Öztop [11] have numerically investigated the heat transfer due to double laminar slot jets impingement onto an isothermal wall within closed long duct. The effect of the jet Reynolds number, the jet-isothermal bottom wall spacing, and the distance between two jets on heat transfer and flow field was examined. They noted that when Reynolds number of the first jet was chosen to be higher than second one, then the heat transfer was enhanced significantly.

Experimental studies on impinging jets have also been conducted. Nirmalkumar et al. [12] have experimentally studied the heat transfer for a flat plate impinged by a slot jet in normal direction. The effects of the jet-to-plate spacing and Reynolds number on the local heat transfer distribution was studied. The Reynolds number based on the slot width was changed from 4200 to 12000 and the jet-to-plate spacing was varied between 0.5 and 12. Thermal images from an infrared thermal camera were used to local heat transfer estimations. The flow field was divided into three regimes; stagnation region, transition region and turbulent wall jet region. Koseoglu and Baskaya [13] have experimentally investigated the effect of the inlet geometry and aspect ratio on the flow and thermal field for different confined imping jet configurations using thermo chromic liquid crystals. Zhou and Lee [14] have experimentally studied the fluid flow and heat transfer of a rectangular air jet impinging on a heated plate. They studied the effects of jet Reynolds number and nozzle-to-plate spacing on the local and average Nusselt numbers. Heat transfer analysis were also conducted in terms of turbulence intensity. Naphon and Wongwises [15] have considered the jet impingement heat transfer for the central processing unit of a personal computer experimentally. The experiments were conducted for three different channel width heat sinks. They noted that, the central processing unit temperature obtained from jet impingement was lower than convectational liquid cooling system. Öztop et al. [16]

have experimentally studied the heat transfer of impinging circular jet onto a heated circular disc. The disc was heated with constant heat flux and it has an inclination. The study was performed for different Reynolds numbers, jet-to-plate distances, jet diameter ratios and inclination angles. They found that the most effective parameter is the inclination angle and both location and stagnation point heat transfer are affected from this parameter.

In heat transfer applications, nano-sized particles (average particle size less than 100 nm) are added in the base fluid such as water or ethylene glycol to obtain better thermal properties compared to base flow. Nanofluids have improved heat transfer characteristics with little pressure drop as compared to base fluids [17]. The study of nanofluids in impinging jets have been conducted by many researchers. Manca et al. [18] have numerically studied the heat transfer and fluid flow of a confined slot impinging jet of water with Al_2O_3 nanoparticles. They used the single phase model and the flow is turbulent. They observed that the intensity and size of the vortex structures depend on the confining effect, Reynolds number and particle size and average Nusselt number increases for increasing particle concentrations and Reynolds numbers. Nguyen et al. [19] have performed an experimental investigation to study the thermal performance of 36 nm Al_2O_3 particle-water nanofluid in a confined and submerged impinging jet on a flat, horizontal and circular heated surfaces. They considered the problem for different range of Reynolds numbers, Prandtl number, distance nozzle-to heated surface and particle volume fractions. Their results have revealed that depending on the combination of nozzle-to-heated surface distance and particle volume fraction, heat transfer enhancement can be obtained in some cases; for other combinations adverse effect of nanoparticles on the heat transfer occur. Li et al. [20] have experimentally studied the single jet impingement cooling using water as the base fluid and Cu particles with 25 nm and 100 nm diameters as additives. The effects of Reynolds number, nanoparticle concentration, nozzle-to-plate distance, nanoparticle diameter on the heat transfer performances of the jet impingement were discussed. They observed that the suspended nanoparticles increase the convective

Table 1
Thermophysical properties.

Property	Water	Al_2O_3
$\rho(\text{kg/m}^3)$	998.2	3880
$c_p(\text{J/kg K})$	4182	773
$k(\text{W/m K})$	0.597	36
$\mu(\text{Pa s})$	993×10^{-6}	–

heat transfer coefficient of the base fluid. The experiments also showed that the suspended nanoparticles brought no extra addition of pressure drop in both submerged single jet impingement. Roy et al. [21] have numerically studied the heat transfer and hydrodynamic characteristics with various types of water based nano-fluids inside a radial cooling device. Different turbulent models and single phase model were used. Heat transfer enhancement were obtained for all nanofluids considered but energy-based performance revealed that they are not the most efficient coolant of this type of application. Yang and Lai [22] have numerically studied the forced convection flow of Al_2O_3 –water nanofluid in the radial flow cooling system. The single phase model was used. Their results showed that when both the cooling performance and the adverse effect of pressure drop are taken into account, no better heat transfer enhancement is found with the use of nanofluid compared to that of pure water.

Even though, there exists studies related to unsteady jets [23,7,5] and pulsating jets [24,25], based on the literature survey and to the best of authors' knowledge a study of pulsating rectangular impinging jet with nanofluids has never been studied. The aim of the present investigation is to explore the effects of various parameters such as Reynolds number, nano- particle volume fraction, pulsating frequency on the heat transfer and fluid flow characteristics for a rectangular impinging jet in the laminar flow regime.

2. Numerical simulation

2.1. Physical problem

A schematic description of the physical problem of computational domain considered in this study is shown in Fig. 1. The two-dimensional model of the physical problem has two plates separated with a distance H and length L . A jet from the rectangular slot on the top plate impinges on the bottom plate. The width of slot is W . The jet has a uniform velocity with a sinusoidal time dependent part $U = U_0(1 + A \sin(2\pi ft))$, for amplitude A and frequency f of the pulsating jet inlet velocity) and a uniform temperature ($T = T_c = 300$ K). The bottom plate is kept at temperature $T = T_h = 310$ K and the top plate is assumed to be adiabatic. It is assumed that thermo-physical properties of the fluid is temperature independent. The flow is assumed to be two dimensional, Newtonian, incompressible and in the laminar flow regime. The effect of the buoyancy is negligible due to the low temperature difference between the bottom plate and incoming jet.

2.2. Thermo-physical properties of the Al_2O_3 –water nanofluid

The working fluid is water with Al_2O_3 nanoparticles (see Table 1). In the present study, single phase or homogeneous model is used. The single phase model assumes that the liquid phase and nanoparticles are in thermal equilibrium and move of same velocity.

The effective thermo physical properties of nanofluids are defined by using the following formulas. The effective density of a

nanofluid can be obtained based on the classical two phase mixture as

$$\rho_{nf} = (1 - \phi)\rho_{bf} + \phi\rho_p. \quad (1)$$

Under the thermal equilibrium conditions, the specific heat of nanofluid is given

$$(C)_{nf} = (1 - \phi)(C)_{bf} + \phi(C)_p, \quad (2)$$

where the subscripts bf, nf and p denote the base fluid, nanofluid and nanoparticle, respectively.

Dynamic viscosity of the nanofluid is computed using the correlation obtained from the least squares curve fitting of the experimental data as Wang et al. [26]

$$\mu_{nf} = \mu_{bf}(123\phi^2 + 7.3\phi + 1). \quad (3)$$

Thermal conductivity of the nanofluid is obtained using the well known Hamilton and Crosser model [27] as,

$$k_{nf} = k_{bf}(4.97\phi^2 + 2.72\phi + 1). \quad (4)$$

2.3. Governing equations and solution method

Considering the local thermal equilibrium, and assuming nanofluid behaves as a conventional single-phase fluid and its properties evaluated as a function of those of both constituents as given above, the continuity, momentum and energy equations can be expressed for two dimensional, incompressible, laminar and unsteady case as in the following.

$$\frac{\partial u}{\partial x} + \frac{\partial v}{\partial y} = 0, \quad (5)$$

$$\frac{\partial u}{\partial t} + u \frac{\partial u}{\partial x} + v \frac{\partial u}{\partial y} = -\frac{1}{\rho_{nf}} \frac{\partial p}{\partial x} + \nu_{nf} \left(\frac{\partial^2 u}{\partial x^2} + \frac{\partial^2 u}{\partial y^2} \right), \quad (6)$$

$$\frac{\partial v}{\partial t} + u \frac{\partial v}{\partial x} + v \frac{\partial v}{\partial y} = -\frac{1}{\rho_{nf}} \frac{\partial p}{\partial y} + \nu_{nf} \left(\frac{\partial^2 v}{\partial x^2} + \frac{\partial^2 v}{\partial y^2} \right), \quad (7)$$

$$\frac{\partial T}{\partial t} + u \frac{\partial T}{\partial x} + v \frac{\partial T}{\partial y} = \alpha_{nf} \left(\frac{\partial^2 T}{\partial x^2} + \frac{\partial^2 T}{\partial y^2} \right), \quad (8)$$

where u , v , T and p represent the two velocity components, temperature and pressure, respectively. ρ_{nf} , ν_{nf} and $\alpha_{nf} (= \frac{k_{nf}}{\rho_{nf} C_{nf}})$ denote the density, kinematic viscosity and thermal diffusivity of the nanofluid, respectively. The viscous dissipation are assumed negligible in the energy equation.

The boundary conditions for the considered problem in dimensional form can be expressed as:

- At the inlet jet section, velocity is unidirectional and sinusoidal, temperature and velocity are uniform

$$-W/2 \leq x \leq W/2, \quad y = H; \\ v = -U_0(1 + A \sin(2\pi ft)), \quad u = 0, \quad T = T_c.$$

- At the top plate, no-slip boundary boundary condition with adiabatic walls are used

$$-L/2 \leq x \leq L/2, \quad y = H; \\ v = 0, \quad u = 0, \quad \frac{\partial T}{\partial y} = 0 \\ W/2 \leq x \leq L/2, \quad y = H; \\ v = 0, \quad u = 0, \quad \frac{\partial T}{\partial y} = 0.$$

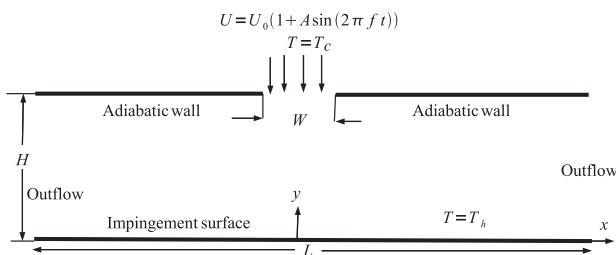


Fig. 1. Geometry with boundary conditions.

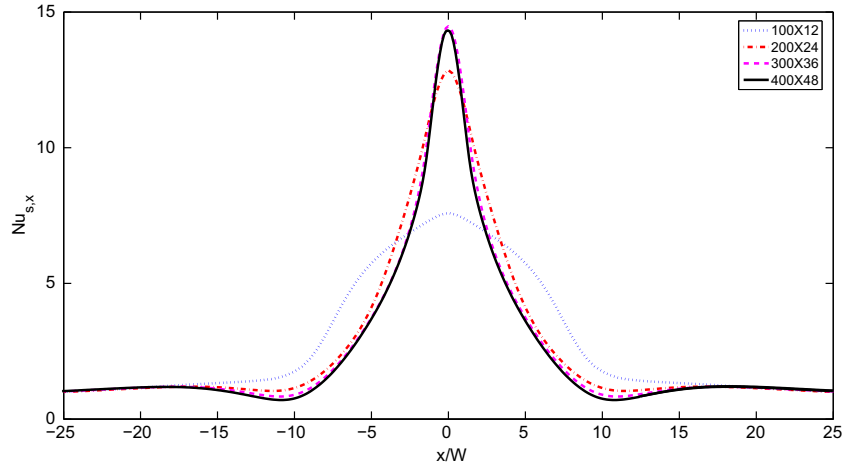


Fig. 2. Local Nusselt number distribution along the bottom isothermal plate for different grid densities at Reynolds number of 200.

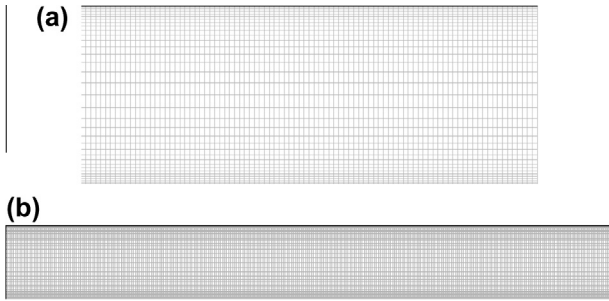


Fig. 3. Mesh distribution for the (b) full computational domain and (a) near the slot.

- At the side surfaces, gradients of all variables in the x -direction are set to zero.

$$0 \leq y \leq H, \quad x = \pm L/2; \\ \frac{\partial v}{\partial x} = 0, \quad \frac{\partial u}{\partial x} = 0, \quad \frac{\partial T}{\partial x} = 0.$$

- At the bottom plate, no-slip boundary condition with constant temperature are used

$$-L/2 \leq x \leq L/2, \quad y = 0; \\ v = 0, \quad u = 0, \quad T = T_h.$$

Local Nusselt number is defined as

$$Nu_{x,t} = \frac{h_{x,t} D_h}{k_{nf}} = - \frac{D_h}{T_h - T_c} \frac{\partial T}{\partial y}_{y=0}. \quad (9)$$

where $h_{x,t}$ represents the local heat transfer coefficient and k_{nf} denotes the thermal conductivity of nanofluid. The hydraulic diameter $D_h = 2W$ is the characteristic length based on the slot width.

Spatial averaged Nusselt number is obtained after integrating the local Nusselt number along the bottom wall as

$$Nu_t = \frac{1}{L} \int_0^L Nu_{x,t} dx. \quad (10)$$

Time and spatial averaged Nusselt number is obtained after integrating spatial averaged Nusselt number along the bottom wall for one period of the oscillation τ as

$$Nu_m = \frac{1}{\tau} \int_0^\tau Nu_t dt. \quad (11)$$

Eqs. (5)–(8) along with the boundary conditions and initial conditions are solved with Fluent (a general purpose finite volume solver [28]). The convective terms in the momentum and energy equations are solved using QUICK scheme and SIMPLE algorithm [29] is used for velocity–pressure coupling. The system of algebraic equations are solved with Gauss–Siedel point by point iterative method and algebraic multi-grid method. The convergence criteria for continuity, momentum and energy equations are set to 10^{-4} , 10^{-6} and 10^{-8} , respectively. The time dependent parts are solved with implicit scheme. Second order implicit time integration is chosen for the temporal discretization. For the unsteady calculations, steady state solutions are used as the initial condition. The computational domain consists of rectangular elements. The mesh is finer near the walls to resolve the high gradients in the thermal and hydrodynamic boundary layer and in the vicinity of and near

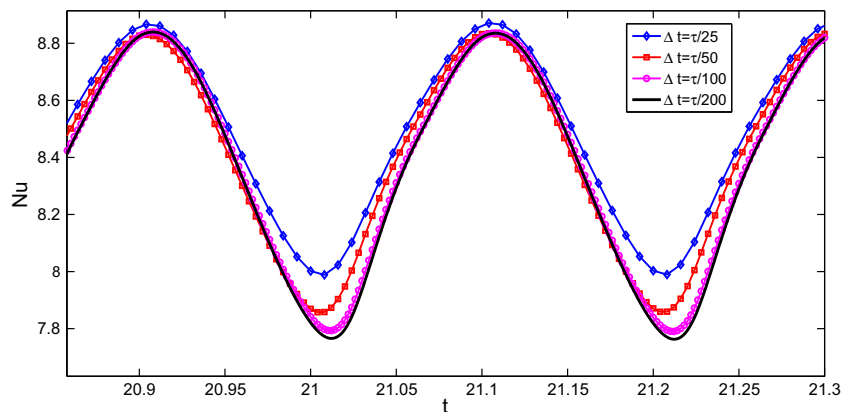


Fig. 4. Time step size independence study.

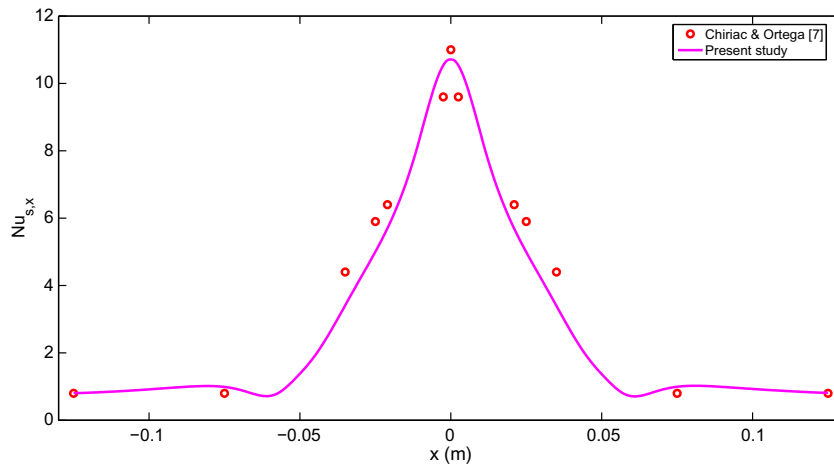


Fig. 5. Comparison of the local Nusselt number distribution along the bottom wall for at Reynolds number of 250 with the results of [7].

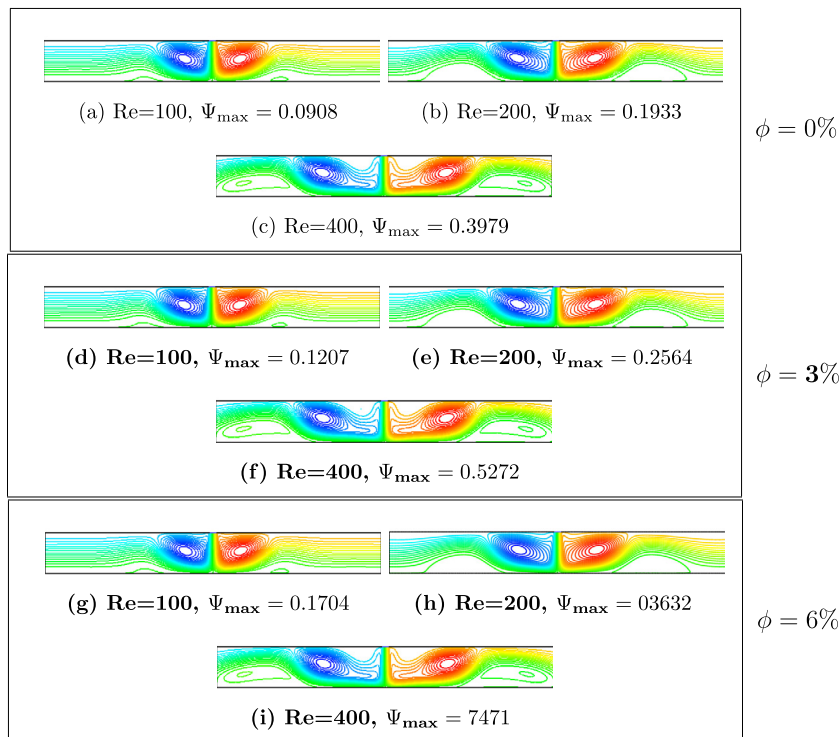


Fig. 6. Streamlines in steady state case for different Reynolds number at volume fraction ϕ of 0 (first box), 3 (second box) and 6% (third box).

the jet flow direction perpendicular to the bottom plate. Mesh independence study is also carried out to obtain an optimal grid distribution with accurate results and minimal computational time. Four different grid sizes are tested and the convergence in the local Nusselt number (along the bottom plate) is checked. The local Nusselt number distribution along the bottom plate for different grid densities at Reynolds number of 200 are shown in Fig. 2. From this figure, grid size of 300×36 is decided to be fine enough to resolve the flow and thermal field for the considered confined rectangular jet impingement problem (see Fig. 3). Time step size independence study is also carried out. Fig. 4 shows the space-averaged Nusselt number along the bottom wall at $Re = 400$, $f = 5$ Hz and $\phi = 0.06$ for different time steps sizes. Time step size $dt = \tau/100$ is chosen both for its accuracy and computational time where τ denotes the period of the oscillation.

The numerical code is first checked against the results problem of confined slot jet impinging on an isothermal surface studied by Chiriac and Ortega [7]. The local Nusselt number distribution along the bottom isothermal plate is shown at Reynolds number of 250 in Fig. 5. The agreement between the maximum Nusselt number and overall Nusselt number is good with the CFD code as compared to the results of [7].

3. Results and discussion

As stated earlier, the overall purpose of this study is to investigate the effects of nanoparticles and pulsating flow on the heat transfer and fluid flow characteristics for different pulsating frequencies and particle volume fractions in the laminar range of Reynolds number between 100 and 400. The main parameters that affect the fluid flow and thermal characteristics are Reynolds

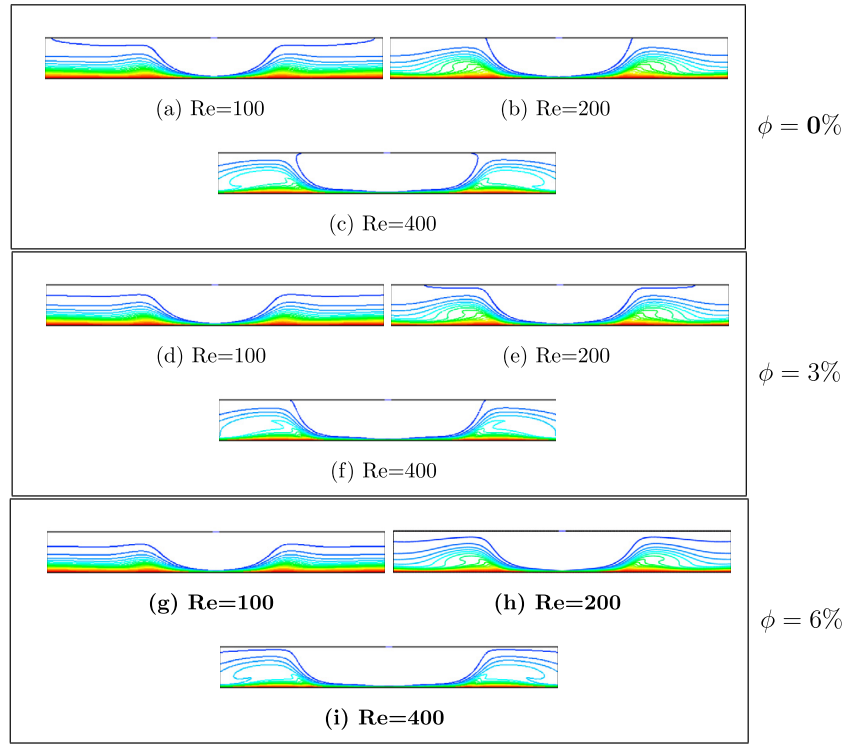


Fig. 7. Temperature contours in steady state case for different Reynolds number at volume fraction ϕ of 0 (first box), 3 (second box) and 6% (third box).

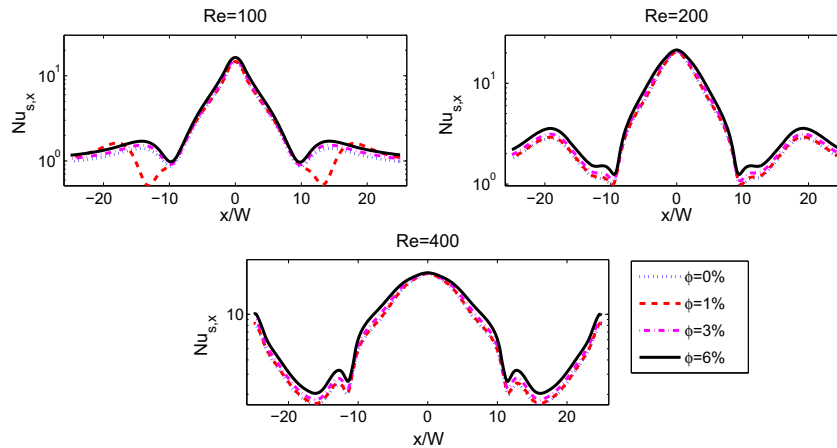


Fig. 8. Variation of local Nusselt number along the bottom plate at various volume fractions for Reynolds number of 100, 200 and 400.

number, nozzle diameter, slot-to-plate spacing, pulsating frequency, amplitude of the pulsating jet inlet velocity, length of the plate, thermal boundary conditions on the bottom plate, velocity of the bottom plate, boundary conditions on the side faces and nanoparticle volume fraction. In the present study, Reynolds number is varied between 100 and 400 and particle volume fraction between 0% and 6%. The ratio of the slot-to-plate distance (H/W) is set to 4 and amplitude of the pulsating jet inlet velocity A is 0.5. The pulsating frequencies f are 1 Hz, 2.5 Hz, 5 Hz and 10 Hz. The length of the plate L is set to $L = 50W$.

3.1. Steady case

Velocity vector plots showing the flow patterns and temperature contours in steady state case at Reynolds number 100, 200 and 400 for different volume fractions are shown in Figs. 6 and 7. As the jet impinges on the hot bottom surface, two counter rotating

vortex are formed due to the jet entrainment and confining effects of the top adiabatic plate. A symmetrical flow with respect to stagnation point is obtained for flow and thermal fields. With increasing the Reynolds number, the size and intensity of the counter rotating cells increase and for $\phi = 0\%$ at $Re = 400$, flow reversal is seen at the exit of the channel. There is slightly change of vector plots for different volume fractions, but the intensity of the vortex are influenced. The temperature gradient is highest and thermal boundary layer is thinnest at the stagnation point and its thickness grows as the normal component of the velocity decreases in the wall jet region. With increasing the volume fraction of the nanoparticles, effective thermal conductivity of the nanofluid increases which result in increase in the fluid bulk temperature.

Variation of the local Nusselt number along the impingement plate for various volume fractions at Reynolds number of 100, 200 and 400 is shown in Fig. 8. Peak values in the Nusselt number is obtained at the stagnation point and its value decreases along

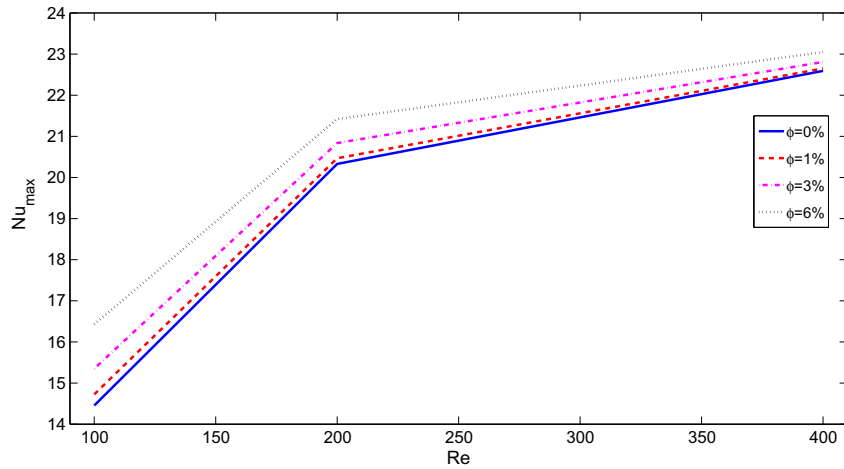


Fig. 9. Variation of stagnation point Nusselt number (maximum) along the bottom plate versus Reynolds number for different volume fractions.

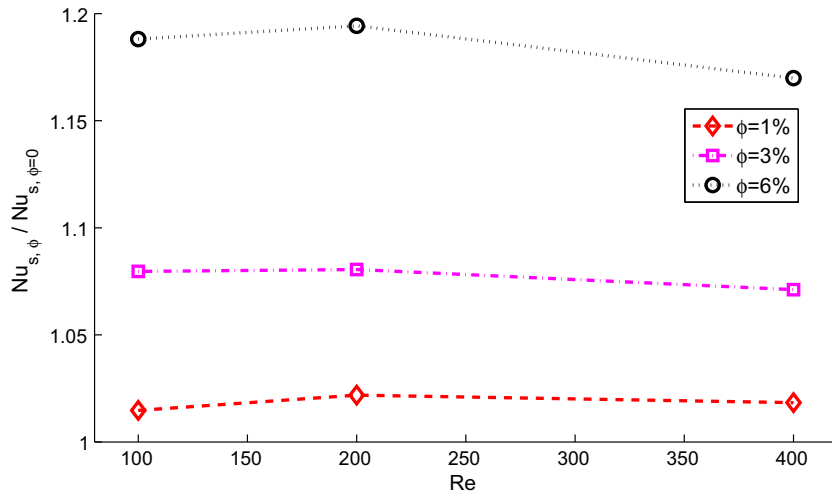


Fig. 10. Variation of spatial-averaged Nusselt number along the bottom plate divided by the spatial averaged Nusselt number for base flow $\phi = 0\%$ versus Reynolds number for different volume fractions.

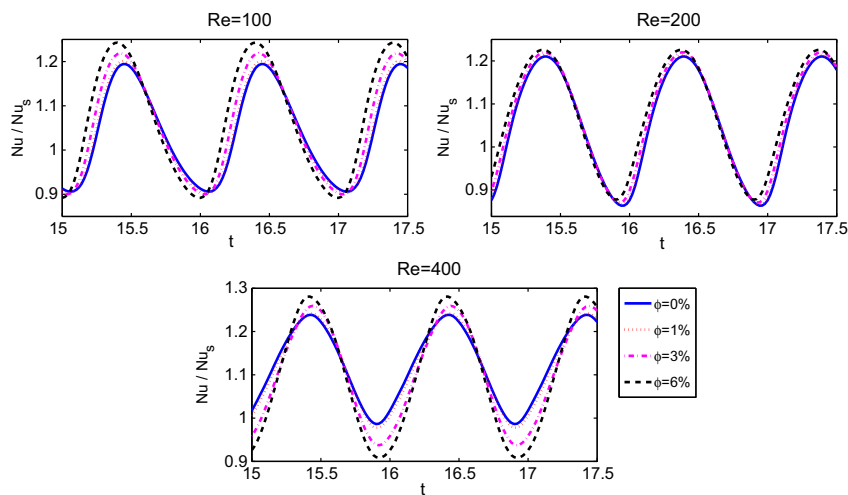


Fig. 11. Time evolution of the spatial-averaged Nusselt number when the steady state periodic oscillations are reached for different volume fractions at Reynolds number of 10, 200 and 400 for pulsating frequency of 1 Hz.

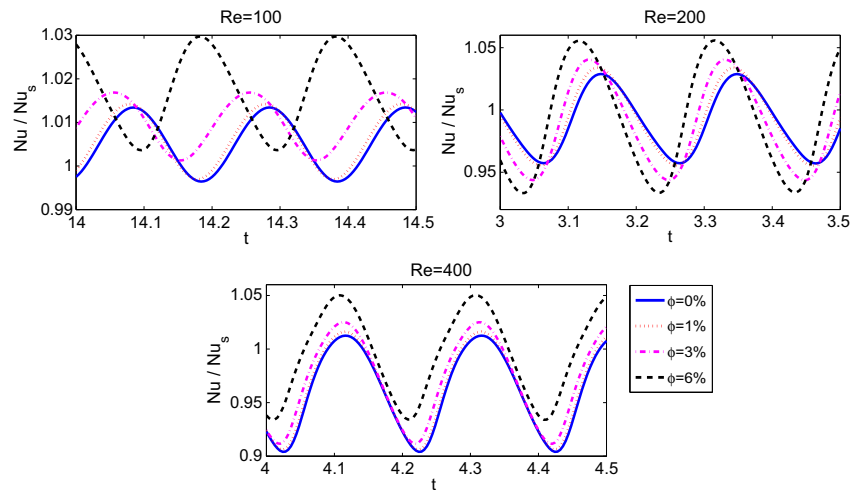


Fig. 12. Time evolution of the spatial-averaged Nusselt number when the steady state periodic oscillations are reached for different volume fractions at Reynolds number of 10, 200 and 400 for pulsating frequency of 5 Hz.

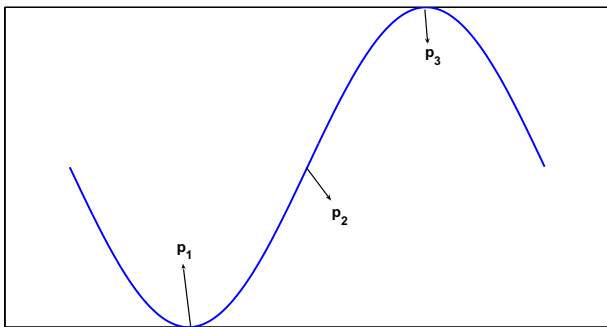


Fig. 13. Three points during the acceleration phase of a half period.

the impingement plate for $Re = 100$. At $Re = 400$, at the exit (ends of the impingement plate), Nusselt number increases due to the thinning of the boundary layer in this region (convection is effective) as can be seen from the temperature contours in Fig. 7. Adding nanoparticles, the peak value in the Nusselt number increases and this increase is more prominent at $Re = 100$ as can be seen from maximum Nusselt number plots in Fig. 9. Fig. 10 shows the relative increase of the average Nusselt number using nanofluids versus

Reynolds number at various volume fractions. As one can see, with increasing the volume fraction, heat transfer enhancement is obtained. The values are 18.8%, 8.1% and 2.2% for $\phi = 6\%$, $\phi = 3\%$ and $\phi = 1\%$, respectively at Reynolds number of 200.

3.2. Transient case

The aim of the present section is to numerically investigate the effects of various pertinent parameters (pulsating frequency, Reynolds number, pulsating frequency) on the transient evolution of the fluid flow and heat transfer characteristics. Time evolution of the spatial-averaged Nusselt number divided with the steady state value when the periodic steady state oscillations are reached for various Reynolds numbers and volume fractions at frequency of 1 Hz is shown in Fig. 11. With increasing the particle volume fraction, there is a shift in the mean and also there is a phase shift where the peak value is seen. At $Re = 100$, the shift in the mean is in the increasing direction whereas at $Re = 400$, the shift in the mean is decreasing direction for volume fractions of $\phi = 3\%$, 6% . At a higher frequency, at frequency of 5 Hz, time evolution of the spatial-averaged Nusselt number divided with the steady state value for different Reynolds numbers and volume fractions is shown in Fig. 12. A first inspection reveals that with increasing the

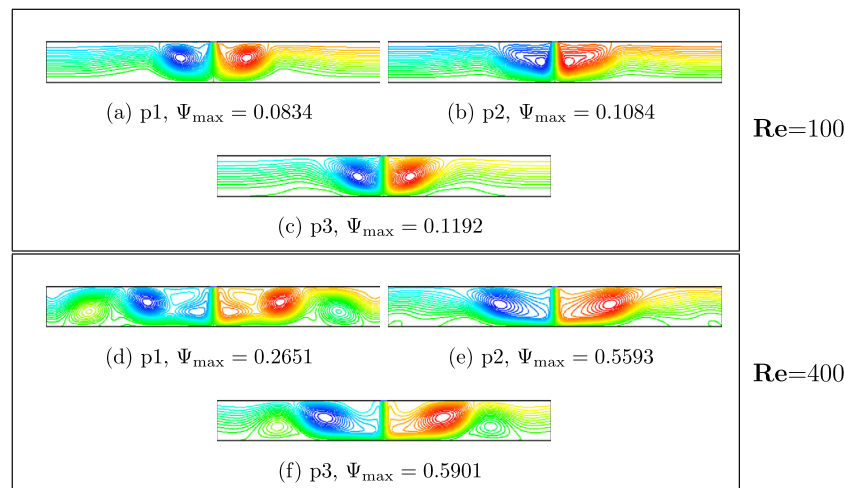


Fig. 14. Streamlines in transient case for different instances of oscillation period during the acceleration phase of the cycle (according to Fig. 11) at Reynolds number of 100 (first box), 400 (second box) for volume fraction of $\phi = 0\%$ and frequency of 1 Hz.

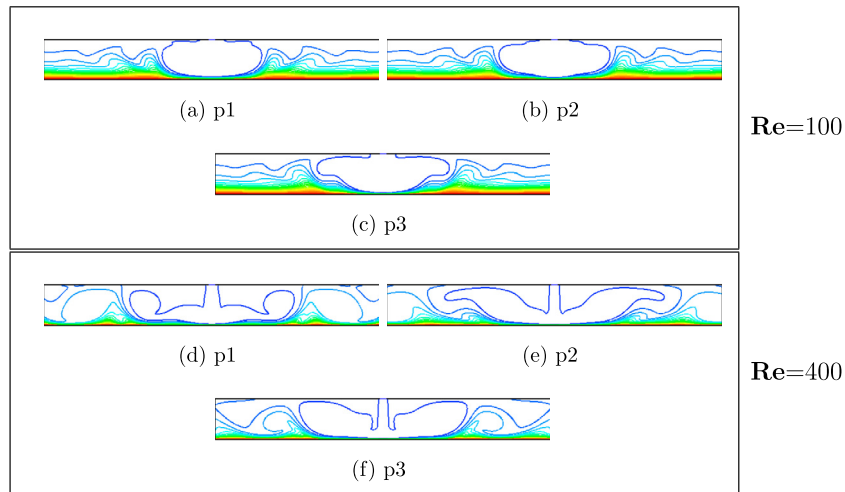


Fig. 15. Isotherm distributions in transient case for different instances of oscillation period during the acceleration phase of the cycle (according to Fig. 5) at Reynolds number of 100 (first box), 400 (second box) for volume fraction of $\phi = 0\%$ and frequency of 1 Hz.

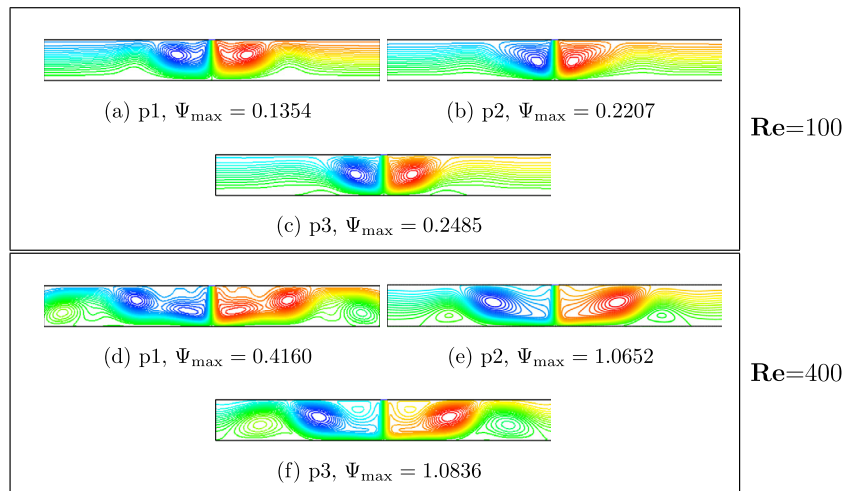


Fig. 16. Streamlines in transient case for different instances of oscillation period during the acceleration phase of the cycle (according to Fig. 5) at Reynolds number of 100 (first box), 400 (second box) for volume fraction of $\phi = 6\%$ and frequency of 1 Hz.

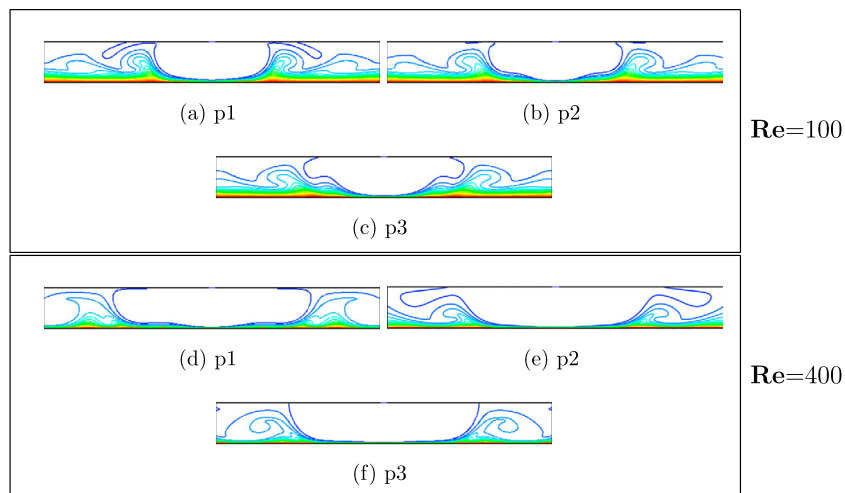


Fig. 17. Isotherm distributions in transient case for different instances of oscillation period during the acceleration phase of the cycle (according to Fig. 5) at Reynolds number of 100 (first box), 400 (second box) for volume fraction of $\phi = 6\%$ and frequency of 1 Hz.

frequency, the peak value in the response (Nusselt number) decreases. This is attributed to the fact that, there is not enough time for the adaption of the flow field to new flow conditions during the ejection of the fluid. There is a considerable phase shift at $Re = 100$ between the base flow and nanofluid with volume fraction of $\phi = 6\%$.

Fig. 13 shows three instances of time during the acceleration phase of a half cycle as denoted by p1, p2 and p3. Fig. 14 shows the velocity vector distribution in transient case for the time instances according to Fig. 13, at Reynolds number of 100 and 400 for volume fraction of $\phi = 0\%$. At $Re = 100$, for the peak point, p3, the flow field is almost the same as in the steady state case, but the intensity of the vortices increase. At $Re = 400$, for the steady state case, the formation of the vortices near the exit is seen which is responsible for the increase of the Nusselt number at the exit. At the time instance for p3, the flow field is the same as in the steady state case, but the core of the cell appeared near the exit above the bottom plate and the core of the main cell adjacent to the jet moves towards the jet. At the time instance for p1, additional vortices are seen above the main cell adjacent to the jet below the top plate.

Temperature contours for three time instances during the acceleration phase of a half period is seen in Fig. 15 for volume fraction of $\phi = 0\%$ at Reynolds number of 100 and 400. At $Re = 100$, as

compared to the steady state case a wavy behavior indicating that convective effects are partly effective. The structure of the isotherms slightly changes in the region adjacent to stagnation point for different time instances at $Re = 100$. At $Re = 400$, there is considerable change in the isotherm patterns when compared to the steady state case. This is due to the formation and distortion of the secondary vortices near the exit and at time instance for p1, the formation of the additional vortices above the main cell adjacent to the jet.

Velocity vector distribution and isotherm plots at $Re = 100$ and $Re = 400$ for particle volume fraction $\phi = 6\%$ for the three time instances according to Fig. 13 are shown in Figs. 16 and 17, respectively. When compared to volume fraction of $\phi = 0\%$, there is slightly change of the velocity vectors near the wall jet region. At $Re = 400$, for $\phi = 6\%$, the additional vortex shown up above the primary cell adjacent to the jet decreases in size and strength when compared to volume fraction of $\phi = 6\%$ at time instance for p1. There is noticeable change in the temperature contours for volume fractions of $\phi = 0\%$ and $\phi = 6\%$. At $Re = 400$, due to the disappearance of additional recirculation pattern above the main cell, the temperature contours near the jet below the top wall seem different at p1 for $\phi = 6\%$ as compared to $\phi = 0\%$.

Variation of the temporal-averaged stagnation point Nusselt number with pulsating frequency for different Reynolds number

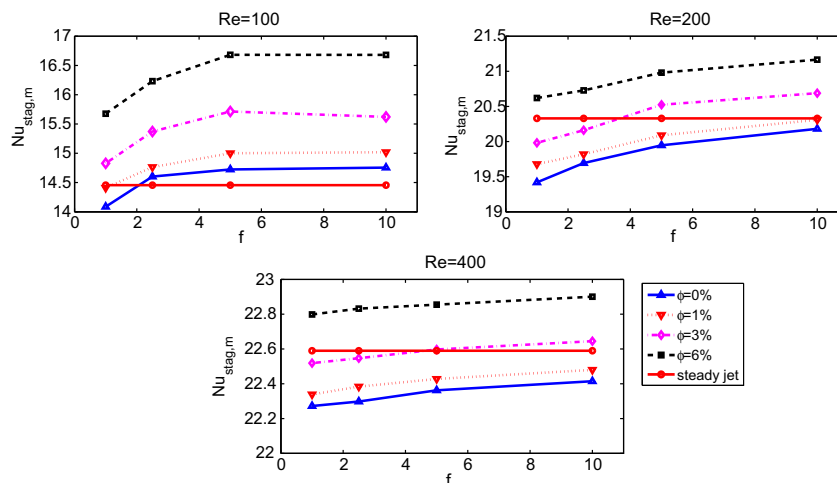


Fig. 18. Variation of the temporal-averaged stagnation point Nusselt number with pulsating frequency for different volume fractions at Reynolds number of 100, 200 and 400.

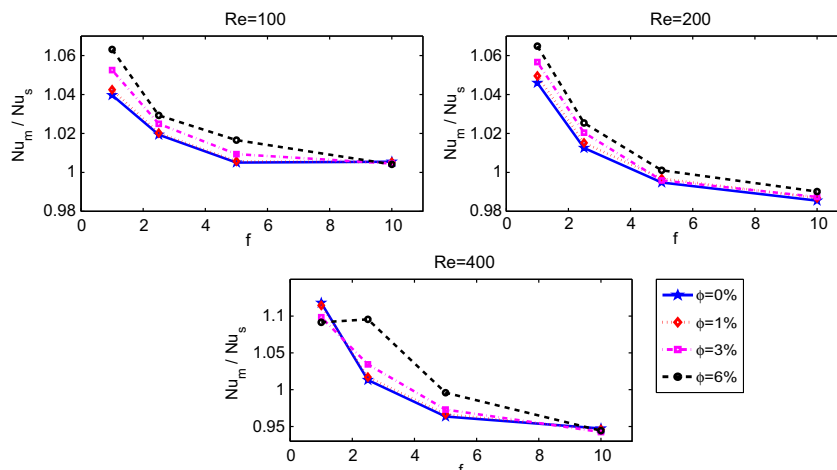


Fig. 19. Variation of the mean Nusselt number with pulsating frequency for different volume fractions at Reynolds number of 100, 200 and 400.

and various volume fractions are shown in Fig. 18. In the plot, the stagnation Nusselt number for the steady jet is also included. The Nusselt values increase with increasing Reynolds number and increasing particle volume fraction for pulsating flow case. The values of the stagnation point Nusselt number are below the steady jet values for volume fraction of $\phi = 0\%$ except for the case at $Re = 100$ and pulsating frequency $f > 1$ Hz. With the inclusion of the nanoparticles at $Re = 100$, the values of the maximum Nusselt number increases with increasing volume fraction. The stagnation point Nusselt numbers generally increase in the direction of increasing frequency, and the nanofluid with a volume fraction of $\phi = 6\%$, has the stagnation point Nusselt number values higher than that of the steady jet for all cases considered. When compared to the study in Ref. [25], the trend in the enhancement of the stagnation point Nusselt number versus frequency of the pulsating flow is similar. In the study of Ref. [25], W/H and amplitude of the pulsation (A) are set to 5 and 0.5 (maximum), respectively. In our study, W/H and A are fixed at 6 and 0.75. The differences in the values are mainly due to the interactions between the jet and the surrounding flow. According to Fig. 9, maximum Nusselt number increases with the addition of the nanoparticles in the direction of increasing volume fraction. From Fig. 18, it is seen that the values of maximum Nusselt number at $Re = 200$, $\phi = 1\%$, 3% and at $Re = 400$, $\phi = 1\%$, 3% are below the steady jet values for low frequencies. This result shows that, the combined effect of pulsation and inclusion of nanoparticles is not favorable for the augmentation of the stagnation point Nusselt number for the considered cases.

Spatial and temporal averaged Nusselt number along the bottom plate versus pulsating frequency are shown for different volume fractions at Reynolds number of 100, 200 and 400 in Fig. 19 (The values are normalized with steady state Nusselt values). As stated earlier, the response decreases with increasing frequency except for the case at $Re = 400$, $f = 1$ Hz for volume fractions of $\phi = 3\%$ and $\phi = 6\%$. This could be attributed to the shift in the mean in decreasing direction with increasing volume fraction as shown in Fig. 11. Heat transfer enhancement is observed with increasing particle volume fraction and this is effective at the low frequency except for the case at $Re = 400$, $f = 1$ Hz.

4. Conclusions

In the current study, numerical simulation of pulsating rectangular jet with the inclusion of the nanoparticles is performed for different particle volume fractions, Reynolds number and pulsating frequency. The effects of various parameters on fluid flow and heat transfer are studied. Following results are obtained:

- Adding nanoparticles in the steady case, the peak value in the Nusselt number (stagnation point Nusselt number) increases and this increase is more effective at $Re = 100$.
- The relative increase of the heat transfer enhancement using nanofluids in steady case is 18.8%, 8.1% and 2.2% for volume fractions $\phi = 6\%$, $\phi = 3\%$ and $\phi = 1\%$, respectively at Reynolds number of 200.
- In the pulsating flow case, the stagnation point Nusselt values increase with increasing Reynolds number and increasing particle volume fraction.
- The stagnation point Nusselt numbers generally increase in the direction of increasing frequency, and the nanofluid with a volume fraction of $\phi = 6\%$, has the stagnation point Nusselt number values higher than that of the steady jet for all cases considered.
- In the steady case, maximum Nusselt number increases with the addition of the nanoparticles in the direction of increasing volume fraction, but for the pulsating flow case the values of

maximum Nusselt number at $Re = 200$, $\phi = 1\%$, 3% and at $Re = 400$, $\phi = 1\%$, 3% are below the steady jet values for low frequencies. This indicates that, the combined effect of pulsation and inclusion of nanoparticles is not favorable for the augmentation of the stagnation point Nusselt number for the considered cases.

- Spatial and time averaged Nusselt number along the bottom plate decreases with increasing frequency except for the case at $Re = 400$, $f = 1$ Hz for volume fractions of $\phi = 3\%$ and $\phi = 6\%$. This could be attributed to the shift in the mean in decreasing direction with increasing volume fraction.
- Heat transfer enhancement is observed with increasing particle volume fraction and this is effective at the low frequency except for the case at $Re = 400$, $f = 1$ Hz.

References

- [1] K. Jambunathan, E. Lai, M. Moss, B. Button, A review of heat transfer data for single circular jet impingement, *Int. J. Heat Fluid Flow* 13 (1992) 106–115.
- [2] B. Webb, C. Ma, Single-phase liquid jet impingement heat transfer, *Adv. Heat Transfer* 26 (1995) 105–217.
- [3] H. Martin, Heat and mass transfer between impinging gas jets and solid surfaces, *Adv. Heat Transfer* 13 (1977) 1–60.
- [4] Y. Chen, C. Ma, M. Qin, Y. Li, Theoretical study on impingement heat transfer with single-phase free-surface slot jets, *Int. J. Heat Mass Transfer* 48 (2005) 3381–3386.
- [5] H. Lee, H. Yoon, M. Ha, A numerical investigation on the fluid flow and heat transfer in the confined impinging slot jet in the low Reynolds number region for different channel heights, *Int. J. Heat Mass Transfer* 51 (2008) 4055–4068.
- [6] T. Park, H. Choi, J. Yoo, S. Kim, Streamline upwind numerical simulation of two-dimensional confined impinging slot jets, *Int. J. Heat Mass Transfer* 46 (2003) 251–262.
- [7] V.A. Chiriac, A. Ortega, A numerical study of the unsteady flow and heat transfer in a transitional confined slot jet impinging on an isothermal surface, *Int. J. Heat Mass Transfer* 45 (2002) 1237–1248.
- [8] Z. Lou, A. Mujumdar, C. Yap, Effects of geometric parameters on confined impinging jet heat transfer, *Appl. Therm. Eng.* 25 (2005) 2687–2697.
- [9] M. Sharif, A. Banerjee, Numerical analysis of heat transfer due to confined slot-jet impingement on a moving plate, *Appl. Therm. Eng.* 29 (2009) 532–540.
- [10] Y. Varol, D.E. Alnak, H.F. Öztop, K. Al-Salem, Numerical analysis of heat transfer due to slot jets impingement onto two cylinders with different diameters, *Int. Commun. Heat Mass Transfer* 39 (2012) 726–735.
- [11] I. Dagtekin, H.F. Öztop, Heat transfer due to double laminar slot jets impingement onto an isothermal wall within one side closed long duct, *Int. Commun. Heat Mass Transfer* 35 (2008) 65–75.
- [12] M. Nirmalkumar, V. Katti, S. Prabhu, Local heat transfer distribution on a smooth flat plate impinged by a slot jet, *Int. J. Heat Mass Transfer* 54 (2011) 727–738.
- [13] M.F. Koseoglu, S. Baskaya, The role of jet inlet geometry in impinging jet heat transfer, modeling and experiments, *Int. J. Therm. Sci.* 49 (2010) 1417–1426.
- [14] D. Zhou, S.-J. Lee, Forced convective heat transfer with impinging rectangular jets, *Int. J. Heat Mass Transfer* 50 (2007) 1916–1926.
- [15] P. Naphon, S. Wongwises, Investigation on the jet liquid impingement heat transfer for the central processing unit of personal computers, *Int. Commun. Heat Mass Transfer* 37 (2010) 822–826.
- [16] H.F. Öztop, Y. Varol, A. Koca, M. Firat, B. Turan, I. Metin, Experimental investigation of cooling of heated circular disc using inclined circular jet, *Int. Commun. Heat Mass Transfer* 38 (2011) 990–1001.
- [17] H.F. Öztop, E. Abu-Nada, Numerical study of natural convection in partially heated rectangular enclosures filled with nanofluids, *Int. J. Heat Fluid Flow* 29 (2008) 1326–1336.
- [18] O. Manca, P. Mesolella, S. Nardini, D. Ricci, Numerical study of a confined slot impinging jet with nanofluids, *Nanoscale Res. Lett.* 6 (2011) 188.
- [19] C.T. Nguyen, N. Galanis, G. Polidori, S. Fohanno, C.V. Popa, A.L. Beche, An experimental study of a confined and submerged impinging jet heat transfer using Al_2O_3 -water nanofluid, *Int. J. Therm. Sci.* 48 (2009) 401–411.
- [20] Q. Li, Y. Xuan, F. Yu, Experimental investigation of submerged single jet impingement using Cu-water nanofluid, *Appl. Therm. Eng.* 36 (2012) 426–433.
- [21] G. Roy, I. Gherasim, F. Nadeau, G. Poitras, C.T. Nguyen, Heat transfer performance and hydrodynamic behavior of turbulent nanofluid radial flows, *Int. J. Therm. Sci.* 58 (2012) 120–129.
- [22] Y.-T. Yang, F.-H. Lai, Numerical study of heat transfer enhancement with the use of nanofluids in radial flow cooling system, *Int. J. Heat Mass Transfer* 53 (2010) 5895–5904.
- [23] Y. Chung, K. Luo, N. Sandham, Numerical study of momentum and heat transfer in unsteady impinging jets, *Int. J. Heat Fluid Flow* 23 (2002) 592–600.

- [24] C. Camci, F. Herr, Forced convection heat transfer enhancement using a self-oscillating impinging planar jet, *ASME J. Heat Transfer* 124 (2002) 770–782.
- [25] T. Demircan, H. Turkoglu, The numerical analysis of oscillating rectangular impinging jets, *Numer. Heat Transfer, Part A* 58 (2010) 146–161.
- [26] X. Wang, X. Xu, S. Choi, Thermal conductivity of nanoparticles–fluid mixture, *J. Thermophys. Heat Transfer* 13 (1999) 474–480.
- [27] R. Hamilton, O. Crosser, Thermal conductivity of heterogeneous two-component systems, *I & EC Fundam.* 3 (1962) 187–191.
- [28] FLUENT User's Guide, Fluent Inc., Lebanon, NH, 2005.
- [29] S. Patankar, *Numerical Heat Transfer and Fluid Flow*, Hemisphere, Washington, DC, 1980.